Available online at www.sciencedirect.com
ScienceDirect
International Journal of Heat and Mass Transfer 51 (2008) 4775–4787
International Journal of HEAT and MASS TRANSFER
www.elsevier.com/locate/ijhmt

Refrigerant flow boiling heat transfer in parallel microchannels as a function of local vapor quality

Stefan S. Bertsch [a,b], Eckhard A. Groll [a,b], Suresh V. Garimella [b,*]

[a] Ray W. Herrick Laboratories, School of Mechanical Engineering, Purdue University, 585 Purdue Mall, West Lafayette, IN 47907-2088, USA
[b] Cooling Technologies Research Center, School of Mechanical Engineering, Purdue University, 585 Purdue Mall, West Lafayette, IN 47907-2088, USA

Received 12 September 2007; received in revised form 14 January 2008
Available online 11 April 2008

Abstract

Flow boiling of refrigerant HFC-134a in a multi-microchannel copper cold plate evaporator is investigated. The heat transfer coefficient is measured locally for the entire range of vapor qualities starting from subcooled liquid to superheated vapor. The test piece contains 17 parallel, rectangular microchannels (0.762 mm wide) of hydraulic diameter 1.09 mm and aspect ratio 2.5. The design of the test facility is validated by a robust energy balance as well as a comparison of single-phase heat transfer coefficients with results from the literature. Results are presented for four different mass fluxes of 20.3, 40.5, 60.8, and 81.0 kg m^{-2} s^{-1}, which correspond to refrigerant mass flow rates of 0.5–2.0 g s^{-1}, and at three different pressures 400, 550 and 750 kPa corresponding to saturation temperatures of 8.9, 18.7, and 29 °C. The wall heat flux varies from 0 to 20 W/cm^2 in the experiments. The heat transfer coefficient is found to vary significantly with refrigerant inlet quality and mass flow rate, but only slightly with saturation pressure for the range of values investigated. The peak heat transfer coefficient is observed for a vapor quality of approximately 20%.

Keywords: Microchannel; Electronics cooling; Flow boiling; Refrigeration; Local heat transfer coefficient

1. Introduction

Boiling heat transfer in microchannels has received significant attention due to its capability for dissipating high heat fluxes especially in the thermal management of microelectronics [1–4], while at the same time minimizing temperature gradients across the chip [5]. The steady increase in gate density over the last few decades has resulted in an associated increase in power dissipation.

Flow boiling of water in single and parallel microchannels has been investigated by several authors [6–11]. In contrast, refrigeration with vapor compression systems [12–14] has received less attention even though it has been shown to be an effective means for lowering the coolant temperature, and therefore, maintaining acceptable device temperatures when dissipating high heat fluxes. The primary advantages of small-scale vapor compression systems are the possibility of achieving fluid temperatures below ambient, a lower freezing point compared to water, and compatibility with electronic circuits in case of leakage due to their higher dielectric strength. In addition, the form factor of such systems, consisting of small heat sinks on the microchip and remote compressor and condenser, is usually quite practical.

Table 1 summarizes several representative studies of refrigerant flow boiling heat transfer from the literature. The working fluids are HFC refrigerants or water, with tests having been conducted either in single or multiple parallel microchannels. Compared to the large number of studies using water [1], flow boiling of refrigerants has been less widely studied. Of these, very few have spanned the complete range of vapor qualities from subcooled liquid to superheated vapor, especially with measurements of local heat transfer coefficients. However, this knowledge is essential in the design and optimization of microchannel cold plate evaporators.

* Corresponding author. Tel.: +1 765 494 5621.
E-mail address: sureshg@purdue.edu (S.V. Garimella).

0017-9310/$ - see front matter © 2008 Elsevier Ltd. All rights reserved.
doi:10.1016/j.ijheatmasstransfer.2008.01.026

Nomenclature

A	area, m^2
G	mass flux, $kg\,m^{-2}\,s^{-1}$
H	fin height, m
h	heat transfer coefficient, $W\,m^{-2}\,K^{-1}$
i	enthalpy, $J\,kg^{-1}$
i_{fg}	latent heat of vaporization, $J\,kg^{-1}$
k	thermal conductivity, $W\,m^{-1}\,K^{-1}$
L	length in flow direction, m
$\dot{m}$	total mass flow rate, $kg\,s^{-1}$
N	number of microchannels
Nu	Nusselt number
P	pressure, Pa
Pr	Prandtl number
q''	heat flux, $W\,m^{-2}$
$\dot{Q}$	heat transfer rate, W
Re	Reynolds number
T	temperature, °C
ΔT_{LMTD}	log mean temperature difference, °C
W	channel width, m
x	vapor quality

Greek symbol

μ	viscosity, $kg\,s^{-1}\,m^{-1}$

Subscripts

3	statepoint 3, pre-evaporator inlet
4	statepoint 4, test piece inlet
5	statepoint 5, test piece outlet
6	statepoint 6, post-evaporator outlet
ave	average
calc	calculated
Ch	Churchill
cond	conduction
cu	copper
fd	developed
el	electrical
f	fluid
in	inlet
out	outlet
preev	pre-evaporator
postev	post-evaporator
ref	refrigerant
sat	saturation
sub	subcooled
ST	Sieder and Tate
test	test piece
tot	total
w	wall

Lazarek and Black [15] found the heat transfer to be independent of the vapor quality in their experiments with vapor qualities as high as 60%. Similar behavior was encountered by Tran et al. [16]. Yan and Lin [17] conducted experiments over the entire vapor quality range, and found very different results: a distinct peak in the heat transfer coefficient near 20% vapor quality at higher saturation temperatures and an almost flat profile at lower evaporation temperatures. Lin et al. [18] observed a qualitatively similar shape of the heat transfer coefficient versus vapor quality with a peak at 10% vapor quality. Lee and Lee [19] and Saitoh et al. [20] found similar behavior to conventional tubes with a trend of increasing heat transfer at higher vapor quality. Finally Steinke and Kandlikar [21] reported a monotonical decrease in heat transfer coefficient with increasing vapor quality. The range of channel hydraulic diameters in these studies varied from 0.5 to 3.1 mm, with the exception of [21] who reported heat transfer for microchannels of 0.207 mm hydraulic diameter.

The present work focuses on investigating the local, vapor quality-based, flow boiling heat transfer coefficients in a microchannel cold plate evaporator through well-characterized experiments. The refrigerant HFC-134a is chosen as the working fluid since it is one of the most suitable choices for microelectronics thermal management applications [12,14]. It is noted that the primary objective of the experiments in this work was to obtain the heat transfer coefficient in flow boiling of a refrigerant through multiple parallel microchannels as a function of refrigerant quality; the width of the microchannels and intervening fins are not optimized to maximize the total heat transfer rate.

2. Experimental setup and data reduction

2.1. Flow loop

Fig. 1 (Top) shows a schematic diagram of the test setup used to investigate heat transfer during refrigerant flow boiling in microchannels. The test setup consists of a hermetically sealed fluid loop with a variable-speed gear pump, the test section assembly in which the refrigerant evaporates, a condenser, several valves to regulate the flow, and instrumentation. In addition, an accumulator with a membrane to separate refrigerant and nitrogen is installed in the loop, which is used to adjust the refrigerant pressure in the setup and serves to damp out flow fluctuations. A refrigerant filter-dryer as well as a 7-μm filter are installed in the flow loop in order to maintain it free from contaminants. A subcooler is used to adjust the subcooling of the refrigerant prior to entering the test section assembly. The condenser as well as the subcooler are tube-in-tube heat exchangers, which are cooled by an externally controlled temperature bath that allows temperature control in the range of −20 to +30 °C.

Table 1
Prior studies of flow boiling in microchannels

Author(s)	Year	Fluid	D_h (mm)	Channel number, geometry	T_{sat} (°C)	G (kg m^{-2} s^{-1})	q''[a] (W cm^{-2})	x[b]	Visualization[c]
Tuckerman and Pease [29]	1981	Water	0.086–0.095	100 rectangular	100	1000–5000	Up to 790 base area	...	No
Yan and Lin [17]	1998	R134a	2	28 circular	5–31	50–200	0.5–2.0 wetted area	0.05–0.85 local	No
Lin et al. [18]	2001	R141b	1	1 circular	39–56	300–2000	1–115 wetted area	0–1 local	No
Lee and Lee [19]	2001	R113	0.78–3.63	1 rectangular	...	50–200	0.3–1.5 wetted area	0.15–0.75 overall	No
Molki et al. [30]	2004	R134a	1.93	1 rectangular	15, 20, 25, 30	100–225	0.8–3.5 wetted area	0.04–0.96 overall	No
Steinke and Kandlikar [9]	2004	Water	0.21	6 rectangular	100	157–1782	Up to 93 base area	<0.0–>1.0 local	Yes
Lee and Mudawar [31,32]	2004	R134a	0.35	53 rectangular	−18 to +25	127–654	31.6–93.8 base area	0.2–0.9 local	No
Lee et al. [33]	2005	Water	0.318–0.903	10 rectangular	100	1000–2400	4.5 base area	Overall	No
Lie and Lin [34]	2005	R134a	2–4	1 annular	10, 15	200–300	0–5 wetted area	...	Yes
Saitoh et al. [20]	2005	R134a	0.51, 1.12, 3.10	1 circular	5, 15	150–450	0.5–3.9 wetted area	0.2–1 local	Yes
Chen and Garimella [35]	2006	FC-77	0.39	24 rectangular	97	160–275	5–70 base area	<0–0.7 overall	Yes
Lie and Lin [36]	2006	R134a	2–4	1 annular	10–15	200–300	0–5.5 wetted area	Subcooled overall	Yes
Yen et al. [37]	2006	R123	0.200–0.214	1 rectangular and circular	...	100–800	0–5 wetted area	0–0.8 overall	Yes
Yun et al. [38]	2006	R410A	1.36–1.44	7–8 rectangular	0, 5, 10	200–400	1.0–2.0 wetted area	0–0.85 overall	No
Liu and Garimella [25]	2007	Water	0.384–0.796	25 rectangular	100	221–1283	Up to 129 base area	0–0.2 local	No
Schneider et al. [39]	2007	R123	0.227	5 rectangular	38–80	622– 1368	21.3 base area	Overall	Yes

[a] Heat flux value and the area upon which it is based.
[b] Vapor quality range and if the measurement was local.
[c] Flow visualization was conducted (yes/no).

Fig. 1 (Bottom) shows the state points of the flow loop in a pressure–enthalpy diagram. The liquid refrigerant is pumped using a variable-speed gear pump from state point 1 to 2. The use of a gear pump obviates the need for refrigeration oil, so that the experiments can be run with pure refrigerant. By using the bypass valve V1 and the flow regulator V2, the refrigerant mass flow rate can be adjusted to the desired value. The refrigerant then passes through a Coriolis-type mass flow meter and a liquid-cooled subcooler in order to achieve sufficient subcooling for all operating conditions. A sight glass immediately prior to the test section assembly provides the ability to check for vapor bubbles in the liquid flow. The test section assembly itself consists of several heated and adiabatic sections.

In the following, experimental setup refers to the complete loop containing the pump, heat exchangers, piping, valves, and the test section assembly, while test section assembly refers to the components located within the dashed line in Fig. 1 (Top), containing the pre-evaporator, test piece, post-evaporator, adiabatic sections, inlet and outlet manifold, and the housing. A detailed drawing of the test section assembly is shown in Fig. 2. The inner part of the test section assembly, without the housing, is referred to as test section, and contains seven elements in the following order in the flow direction: inlet manifold, pre-evaporator, adiabatic section, test piece, adiabatic section, post-evaporator, and outlet manifold. Finally, the test piece is the single heated copper block in the middle of the test section, on which most of the actual measurement and analysis is performed.

The refrigerant evaporates in the pre-evaporator from state point 3 to 4, which provides the desired inlet quality for the test piece. The actual test piece is located between state points 4 and 5, where the local heat transfer coefficient is measured for a nominal change in quality of 20%. After leaving the test piece, the refrigerant is heated to state point 6 in the post-evaporator so that the refrigerant reaches a superheated state. The refrigerant is then cooled back to state point 1 in the liquid-cooled condenser.

Pre- and post-evaporators are necessary to calculate the refrigerant quality at the inlet and outlet of the test section assembly via energy balances. Ensuring the presence of single-phase fluid at the entrance and exit of the microchannels also allows for a more even flow distribution than in the case of a two-phase refrigerant entering or leaving the channels. In addition, this setup allows for three redundant means of determining the heat flux, via energy balance, conduction analysis in the copper block,

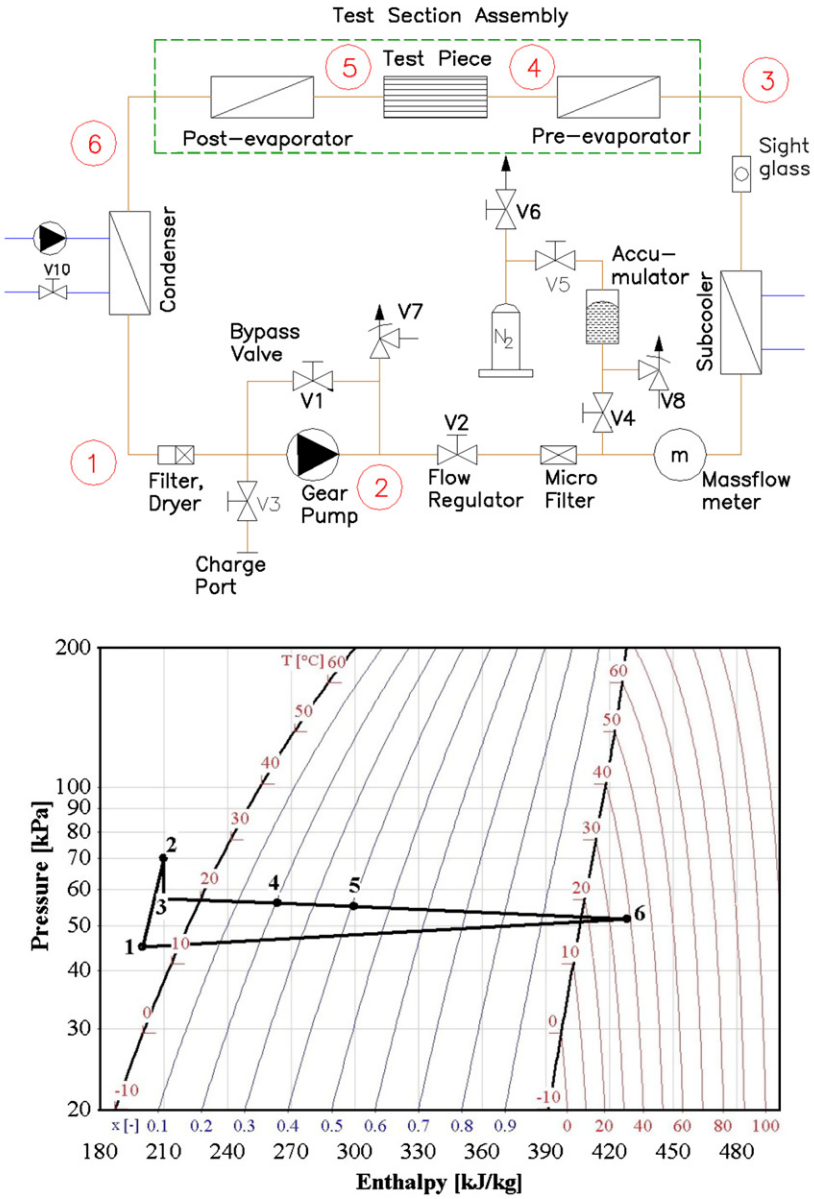

Fig. 1. Experimental setup for vapor quality based investigation of flow boiling in microchannels. Top: schematic of the test loop. Bottom: corresponding state points in a pressure–enthalpy diagram with pre-evaporator, test piece and post-evaporator located in between state points 3, 4, 5 and 6, respectively.

and electrical input power measurement. The inlet quality of the refrigerant in the test piece can be changed by varying the heat input provided by the pre-evaporator. Three independent sets of cartridge heaters with adjustable input power are used in the pre-evaporator, test piece and post-evaporator to provide heat input.

The inlet and outlet sections of the test section assembly as well as the adiabatic sections that are located in between the three heated blocks are made of a thermoplastic (PEEK) which is easy to machine, has a low thermal conductivity ($0.25\,W\,m^{-1}\,K^{-1}$), and has good chemical resistance to the working fluid, HFC-134a. The heated blocks (pre-evaporator, test piece and post-evaporator) are made of oxygen-free copper and contain the cartridge heaters and several thermocouples. Air pockets are located in between the PEEK and copper pieces to increase thermal isolation. A 0.5 mm thick, transparent silicone sheet on top of the microchannels prevents cross-leakage from one channel into the next. The cover plate is made of polycarbonate and allows optical access to the test section from the top. In order to allow for sufficient thermal expansion of the materials, the assembly is compressed with rubber sheets on the side and bottom (part G in Fig. 2 (Top)). An air gap was maintained in between the sides of the test section and the side wall of the casing for the purpose of insulation. In addition air gaps were introduced between all pieces of the test section in the form of small recesses, as shown in Fig. 2 (Top). These gaps and recesses were also used for exact alignment of the microchannels.

The microchannels were cut into the test piece using a jeweler's saw, ensuring that the microchannels across the

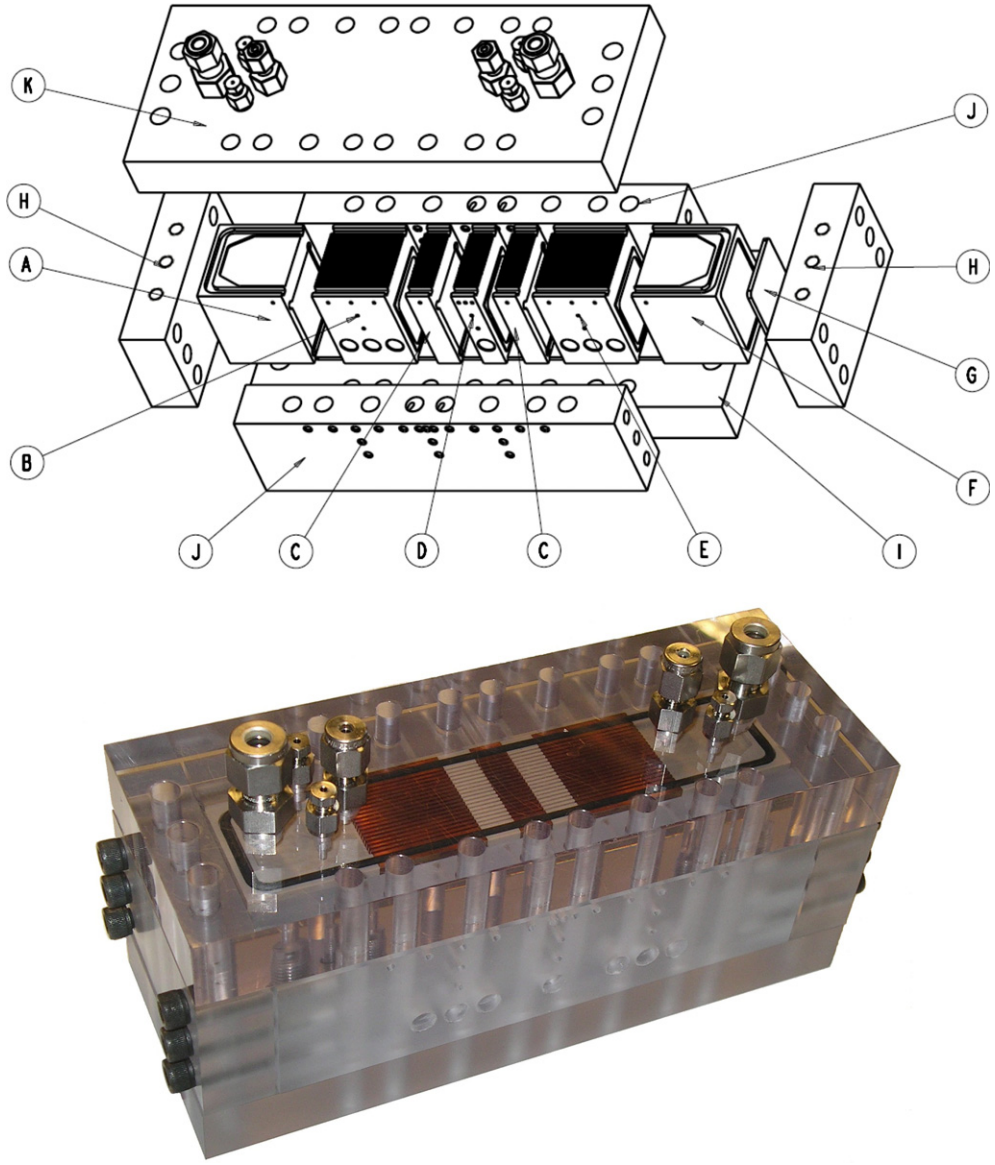

Fig. 2. Test section assembly. Top: exploded view with the components (A) inlet piece, (B) pre-evaporator, (C) adiabatic piece, (D) test piece, (E) post-evaporator, (F) outlet piece, (G) rubber compression, (H) front and back pieces, (I) bottom piece, (J) side pieces, and (K) top piece with fluid ports and bottom: picture of the assembly.

various test section components were well-aligned and matched in size. The resulting surface roughness was measured to be 0.6–0.7 μm for the heated and adiabatic pieces. Only minor changes in channel width were caused due to different re-expansion of the material after cutting the channels. The mismatch in channel width and depth was never greater than 2 μm. Table 2 lists the dimensions of the investigated microchannels together with the measurement and fabrication uncertainties. As can be seen, the only geometrical difference in the microchannels between the three heated sections is the different lengths in the flow direction.

The temperature measurements in all heated blocks were carried out with sheathed thermocouples with a diameter of 0.81 mm and an immersion depth of 9.5 mm assembled in a T-shape as can be seen in Fig. 2. In each heated block, three thermocouples were positioned along the centerline in the direction of heat flow. The thermocouple beads were located at distances from the bottom of the microchannels of 2.1, 10.0 and 17.9 mm, respectively. In addition, the temperature profile along the flow direction was measured with two additional thermocouples positioned 2.1 mm below the bottom of the microchannels. The measurements are carried out with a total of 10 thermocouples per heated block. These thermocouples were also used to calculate the surface temperature by extrapolation.

As mentioned earlier, the fluid loop contains pure refrigerant with no oil. In order to ensure the highest possible purity of the working fluid, the loop was flushed with dry nitrogen and then evacuated several hours every time before charging.

Table 2
Dimensional details of the microchannel test piece

Dimension	Measurement
Number of channels [–]	17
Hydraulic diameter [μm]	1089 ± 2.6
Channel depth [μm]	1905 ± 10
Fin width [μm]	762 ± 2
Channel width [μm]	762 ± 2
Aspect ratio (depth/width) [–]	2.5
Length (test piece) [mm]	9.53 ± 0.02
Length (pre-evaporator) [mm]	30.16 ± 0.02
Length (post-evaporator) [mm]	30.16 ± 0.02
Length (adiabatic sections) [mm]	9.53 ± 0.02
Roughness copper [μm]	<0.6
Roughness (adiabatic sections) [μm]	<0.7
Misalignment [μm]	<2.0

2.2. Data acquisition and uncertainties

A total of approximately 80 temperature and pressure sensors are installed in the experimental setup. The electrical power to the DC cartridge heaters is calculated using voltage and current measurements from a shunt resistor, which leads to an uncertainty of 1.5%. The refrigerant mass flow rate is measured using a Coriolis-type mass flow meter with an uncertainty of 0.2% of the reading within the measurement range. Pressures at different points in the setup are measured using absolute pressure transducers with a range of 170 kPa and an accuracy of 0.25% of full scale. For the differential pressure measurement over the test section, a transducer with a range of 7 kPa and an uncertainty of 0.1% of full scale was used. All temperatures are measured using calibrated T-type thermocouples with an uncertainty of ±0.5 °C. Each reported measurement is obtained as an average of approximately 45 points obtained over 8 min of steady-state data. A standard error analysis [22] was used to estimate the uncertainties in the reported results. The average and maximum uncertainty in the local heat transfer measurements was 7.9% and 11.8%, respectively, with the lowest uncertainty being achieved under subcooled conditions and the highest at low flow rates and low heat fluxes in the saturated flow boiling regime. The average and maximum uncertainties in vapor quality were 1.2% and 2.1%, respectively; these values for the heat flux calculation were 2.8% and 3.0%, respectively.

In addition to the instrumentation discussed above, a camcorder was positioned above the test section assembly to visually observe the flow.

2.3. Test conditions

Measurements were first conducted for single-phase heat transfer in order to establish an energy balance over the entire test section assembly and thus quantify heat gains and losses. These results were also used to validate the heat transfer coefficient measurements, since the heat transfer coefficient in single-phase flow through microchannels is readily predicted. These measurements were carried out with highly subcooled liquid at an outlet pressure of 750 kPa, and flow rates between 10 and 15 g s^{-1} ($Re_f \approx 3000$–4000). The electrical heat input to the test piece was varied from 0 to 150 W, while the pre-evaporator and post-evaporator were turned off in these experiments.

The second set of measurements was carried out to establish a boiling curve. Again, only the test piece itself was heated and the liquid at the inlet was highly subcooled. The electrical input power ranged from 0 to 100 W. With the pressure held constant at 750 kPa, the mass flux was adjusted to values of 20.3, 40.5, 60.8, and 81.0 kg m^{-2} s^{-1} ($Re_f \approx 100$–500).

The flow boiling heat transfer coefficient measurements as a function of local vapor quality were obtained at three pressures (400, 550 and 750 kPa) and four mass fluxes (20.3, 40.5, 60.8, and 81.0 kg m^{-2} s^{-1}). The three pressures correspond to saturation temperatures of 8.9, 18.7, and 29.0 °C. The mass fluxes correspond to mass flow rates ranging from 0.5 to 2.0 g s^{-1}, and roughly to cooling capacities of 100, 200, 300, and 400 W. Several inlet flow conditions for the test piece starting from subcooled liquid all the way to two-phase flow with 80% vapor quality were tested. The quality change undergone by the refrigerant within the test piece was controlled to be 20% (±1%). This choice of 20% quality change is a compromise between measurement accuracy and resolution of the heat transfer coefficient behavior. A total of more than 130 data points have been obtained for the work reported here. In all cases, the refrigerant was subcooled at the test section assembly inlet and superheated at the test section assembly outlet in order to establish an energy balance.

2.4. Data reduction

In order to quantify the refrigerant qualities at the different state points of the system according to Fig. 1, the equations listed in this section were used. The enthalpy at the inlet and outlet of the test section assembly is defined by the pressure and temperature assuming that the inlet and outlet state are in the single-phase regime

$$\begin{aligned} i_3 &= f(T_3, P_3) \\ i_6 &= f(T_6, P_6) \end{aligned} \tag{1}$$

Knowing the enthalpy of the saturated liquid

$$i_{f,sat} = f(P_3, x = 0) \tag{2}$$

the thermodynamic quality can be defined at all state points as follows:

$$x_3 = \frac{i_3 - i_{f,sat}}{i_{fg}}$$
$$x_4 = x_3 + \frac{\dot{Q}_{el,preev}}{\dot{m}_{ref} \cdot i_{fg}} \quad (3)$$
$$x_5 = x_4 + \frac{\dot{Q}_{el,test}}{\dot{m}_{ref} \cdot i_{fg}}$$

Most of the heat transfer results are reported with respect to the local test piece quality $x_{test,loc}$ or the pre-evaporator outlet quality $x_{preev,out}$ which are defined as

$$x_{test,loc} = \frac{x_4 + x_5}{2} \quad (4)$$
$$x_{preev,out} = x_4$$

The heat transfer coefficient in the test piece and the pre-evaporator are defined as

$$h_{test,loc} = \frac{q''_{w,test}}{\Delta T_{w,f,test}} \quad (5)$$
$$h_{preev,ave} = \frac{q''_{w,preev}}{\Delta T_{w,f,preev}}$$

where the wall heat flux is defined for the heated wetted area as

$$q''_{w,test} = \frac{\dot{Q}_{el,test}}{N \cdot L_{test} \cdot (W + 2 \cdot H)} \quad (6)$$
$$q''_{w,preev} = \frac{\dot{Q}_{el,preev}}{N \cdot L_{preev} \cdot (W + 2 \cdot H)}$$

Due to the short length of the test piece, changes in the wall temperature along the flow direction could not be determined; instead, the test piece wall is assumed isothermal which is justified under the largely saturated fluid conditions encountered. In addition, the temperature along the fins is assumed constant, due to the relatively high fin width of 762 μm compared to its height of 1905 μm, leading to fin efficiencies of 96.5–99.9% across the entire set of experiments including single-phase and two-phase measurements. The temperature variation in the test piece in the lateral direction was determined using steady-state thermal simulations using a commercial available computational fluid dynamics software package. The results showed a lateral distribution in the wall temperature over all the interior channels of 0.3 °C. Only the outermost fins on either side showed a temperature deviation compared to the mean base temperature of up to 1 °C in the worst-case scenario (case with the highest heat transfer coefficient) due to the geometry of the setup.

The pressure drop across the test section assembly consisting of the pre-evaporator, test piece and post-evaporator was always below 0.3 kPa, which corresponds to a change in saturation temperature of approximately 0.2 °C. Therefore, the saturation temperature of the refrigerant was assumed to be constant along the length of the test piece, which represents only one-tenth of the length of the test section assembly. The saturation temperature was calculated using the mean pressure between the inlet and outlet of the test section.

Since the refrigerant enters the test piece in some cases as subcooled liquid, the length of the channel can be divided into two regions: the upstream subcooled region and the downstream saturated region. Fig. 3 shows a schematic representation of the fluid temperature variation along the microchannel. As mentioned earlier, the wall temperature and the saturation temperature stay constant over the length of the test piece in the downstream saturated region. The fluid temperature profile in the subcooled region has been assumed to be linear in most studies in the literature (dashed line). In the present work, the temperature difference in the subcooled region is calculated using the log mean temperature difference (LMTD), which is more physically realistic than the assumption of linear temperature variation. The average difference in the heat transfer coefficient calculated using the two methods is 1.4%, with a maximum value of 14.2%.

Using these assumptions and definitions, the effective temperature difference between the wall and fluid can be calculated in the case of subcooled liquid ($x_4 < 0$) at the test piece inlet as follows:

$$\Delta T_{w,f} = \frac{L_{sub} \cdot \Delta T_{LMTD} + (L_{test} - L_{sub}) \cdot (T_w - T_{sat})}{L_{test}} \quad (7)$$

Using

$$\Delta T_{LMTD} = \frac{(T_w - T_{sat}) - (T_w - T_{in})}{\ln\left(\frac{T_w - T_{sat}}{T_w - T_{in}}\right)} \quad (8)$$

and

$$L_{sub} = L \cdot \left(\frac{x_4}{x_4 - x_5}\right) \quad (9)$$

If the fluid is at saturation conditions all the way from the inlet, the following simplified expression can be used to calculate the temperature difference:

$$\Delta T_{w,f} = T_w - T_{sat} \quad (10)$$

A similar procedure (Eqs. (7)–(10)) is used for data reduction for the pre-evaporator. In the case of superheated gas leaving the test piece, the calculation is performed by dividing into saturated and superheated regions instead of the subcooled and saturated regions.

To establish the validity of the experimental determination of the heat transfer coefficient with the given test setup, the energy balance obtained in the test section assembly was first evaluated for single-phase flow. Single-phase flow was chosen since the state points at the inlet and outlet of the test piece are easily defined from known temperatures and pressures. Using these state points and the refrigerant mass flow rate, the heat transfer rate into the test piece can be calculated as follows:

$$\dot{Q}_{out} - \dot{Q}_{in} = \dot{m}_{ref}(i_6 - i_3) \quad (11)$$

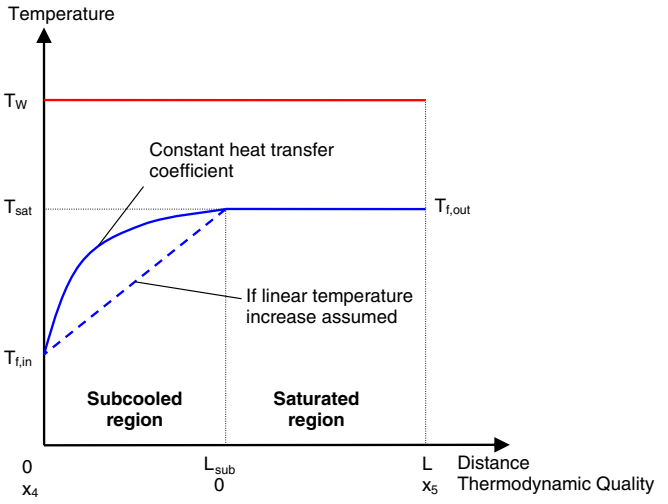

Fig. 3. Schematic representation of the fluid and wall temperature variation along the test piece.

An alternative calculation of the overall heat transfer rate is based on adding the electrical power supplied to the three heated blocks

$$\dot{Q}_{\mathrm{el,tot}} = \dot{Q}_{\mathrm{el,preev}} + \dot{Q}_{\mathrm{el,test}} + \dot{Q}_{\mathrm{el,postev}} \tag{12}$$

A third approach for calculating the heat input is to use the known thermal conductivity and dimensions of each heated copper block together with the temperature difference in the heat flow direction measured with the thermocouples inserted into the heated block

$$\dot{Q}_{\mathrm{cond}} = \frac{k_{\mathrm{cu}} \cdot A_{\mathrm{cu}} \cdot \Delta T_{\mathrm{cu}}}{L_{\mathrm{cu}}} \tag{13}$$

The total heat transfer rate is then calculated by adding the heat transfer rates of the three heated blocks

$$\dot{Q}_{\mathrm{cond,tot}} = \dot{Q}_{\mathrm{cond,preev}} + \dot{Q}_{\mathrm{cond,test}} + \dot{Q}_{\mathrm{cond,postev}} \tag{14}$$

The heat transfer rates calculated by using each of these three methods – Eqs. (11), (12) and (14) – can then be compared as is done with the results in the next section.

The single-phase heat transfer measurements are compared to predictions from the Churchill [23] correlation, valid for $Re < 10^4$ and the Sieder and Tate [24] correlation for turbulent flow since the Reynolds numbers in the experiments varied from 2500 to 3000. From the Nusselt number $Nu_{\mathrm{fd,Ch}}$ calculated according to the Churchill correlation and the Nusselt number $Nu_{\mathrm{fd,ST}}$ from Sieder and Tate, the heat transfer coefficient can be calculated as

$$h_{\mathrm{calc}} = \frac{Nu_{\mathrm{fd}} k_{\mathrm{f}}}{D_{\mathrm{h}}} \tag{15}$$

where Nu_{fd} is substituted with either $Nu_{\mathrm{fd,Ch}}$ or $Nu_{\mathrm{fd,ST}}$ and then compared to the measured heat transfer coefficient. Due to the length of the preheater and adiabatic section being approximately 40 times longer than the hydraulic diameter of the channels, the flow field in the test piece may be considered to be fully developed.

3. Experimental results

3.1. Energy balance

Fig. 4 shows the energy balance calculations in the test section assembly. The heat transfer rate is calculated by three independent means, using Eqs. (11), (12) and (14). As can be seen in Fig. 4, the maximum deviation between the three approaches is 7 W, while the average deviation is 3 W; the maximum uncertainty in heat transfer rate is therefore 5.6% while the average is 2.4% of the maximum heat transfer rate encountered. The measurements cannot be distinguished within the uncertainty range, pointing to the robustness of the experiment design, instrumentation, and measurement accuracy. Due to the excellent energy balance, heat losses are neglected in this study.

3.2. Validation of single-phase results

The measured single-phase heat transfer coefficients are compared with predictions from the Churchill and Sieder–Tate correlations in Fig. 5 and plotted as a function of heat flux. It can be seen that the measured heat transfer coefficients match the predictions to within experimental uncertainty at the lower heat fluxes. As the heat flux (based on the wetted, heated area) exceeds 6 W cm^{-2}, the measured heat transfer coefficients deviate due to the onset of subcooled boiling in the experiments, which leads to far larger heat transfer coefficients than in single-phase flow. For all the results displayed in Fig. 5, the heat transfer coefficient is calculated based on the temperature difference between the fluid and the surface as shown in Eq. (8). Even after the onset of nucleate boiling, bubbles were not visually observed due to the large mass fluxes, and are expected

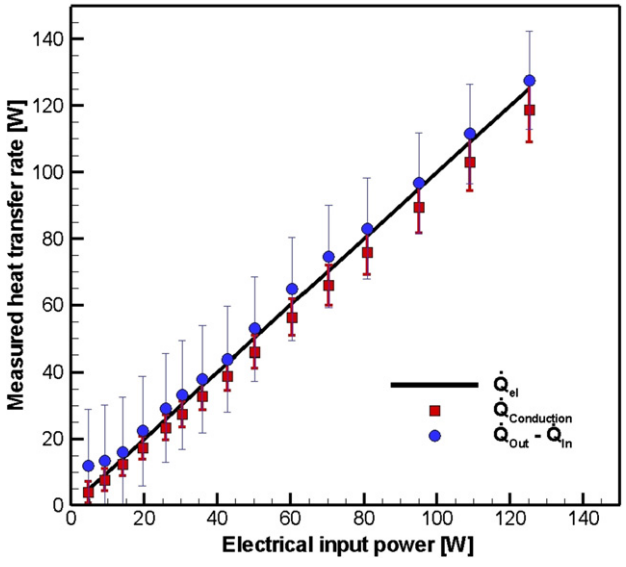

Fig. 4. Energy balance over the test section assembly using electrical input power, heat transfer rate calculated by conduction in the copper block, and heat addition calculated over inlet and outlet enthalpy.

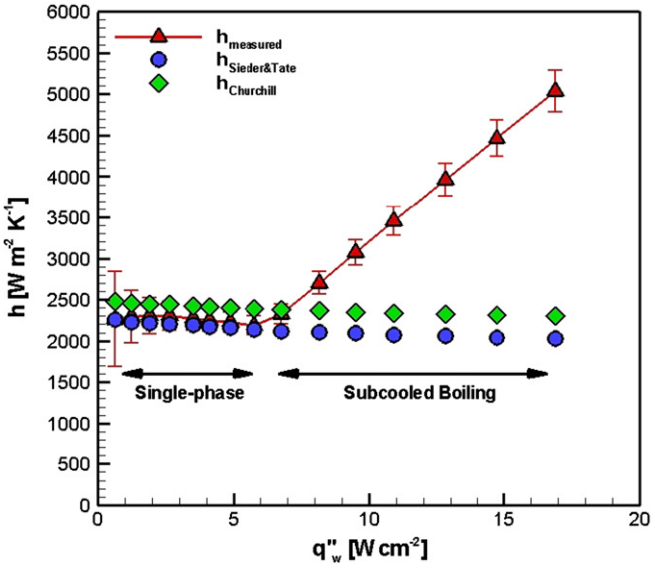

Fig. 5. Measured single-phase heat transfer coefficient compared to predictions from the Churchill [23] and the Sieder and Tate [24] correlations.

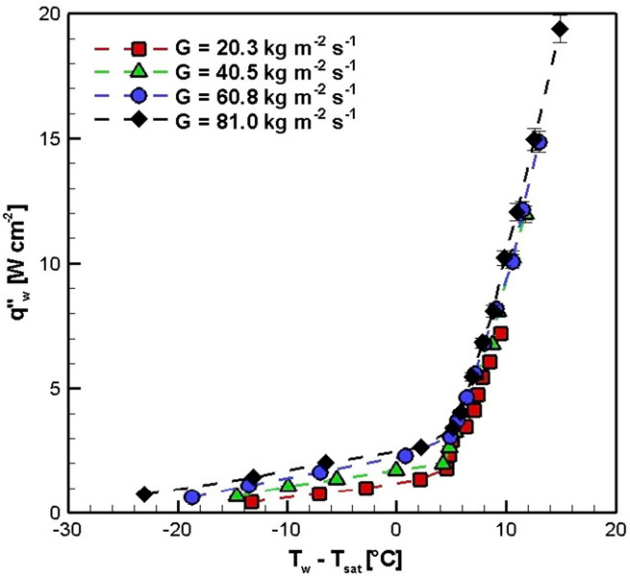

Fig. 6. Boiling curve at a pressure of 750 kPa and four mass fluxes from 20.3 to 81.0 kg m^{-2} s^{-1}.

to have collapsed immediately due to the high degree of subcooling. Onset of subcooled boiling was indicated in the experiments by a slight temperature drop at the surface and a resulting increase in heat transfer coefficient.

3.3. Boiling curve

In order to characterize single-phase heat transfer and subcooled boiling, a boiling curve was constructed from the measurements in the test piece. The results are plotted in terms of the variation of wall heat flux with temperature difference between the wall and saturation temperature in Fig. 6. The saturation pressure was held constant at 750 kPa and the inlet temperature varied slightly with the mass flow rate: at mass fluxes of 20.3, 40.5, 60.8 and 81.0 kg m^{-2} s^{-1}, the inlet temperatures were 2, −1, −3, and −5 °C, respectively. The mass flux was treated as an independent variable to determine its effect on heat transfer. It is observed from Fig. 6 that in the single-phase region, the higher mass flow rate leads to a greater heat dissipation while maintaining the same wall superheat. However, after the onset of nucleate boiling (ONB), all boiling curves collapse onto a single curve irrespective of the inlet temperature and mass flow rate, indicating the dominance of nucleate boiling over convective heat transfer. No significant temperature overshoot at ONB could be detected, as was also the observation for similar boundary conditions in [25]. The flow patterns visually observed after the onset of boiling revealed a mostly bubbly flow regime, which sometimes transitioned to slug flow at the highest measured heat fluxes. Only at the highest heat flux considered, the onset of out-of-phase flow instabilities (fluid in adjacent channels oscillates in opposing directions) as described by [26] was observed.

3.4. Average heat transfer coefficients

While the primary thrust of this work was to obtain the heat transfer coefficient as a function of vapor quality (as discussed in the next section), heat transfer measurements were also obtained as a function of outlet vapor quality, as has been commonly reported in the literature for different fluids and geometries [34–36,39]. The inlet temperature of the refrigerant was kept at -8.3 ± 0.5 °C during all measurements, which is well below the saturation temperatures of 8.9, 18.7, and 29.0 °C. Figs. 7 and 8 show the heat transfer coefficient with respect to outlet vapor quality and heat flux – these measurements were obtained in the section designated 'pre-evaporator', which, for these measurements, functions as a regular microchannel heat sink. The results in Fig. 7 are presented for four different mass fluxes of 20.3, 40.5, 60.8 and 81.0 kg m^{-2} s^{-1} at a constant pressure of 550 kPa. The heat flux is independent of the mass flux and ranges from 0 to approximately 15 W cm^{-2}. Fig. 8 shows results for a constant mass flux of 40.5 kg m^{-2} s^{-1} (flow rate of 1.0 g s^{-1}) and three different saturation pressures of 400, 550, and 750 kPa. The heat transfer coefficients presented are the averaged values from subcooled liquid to the outlet quality shown in the plot.

The results show a strong dependence of the heat transfer coefficient on the vapor quality and heat flux. Inspection of Fig. 7 indicates that the heat transfer coefficient increases with increasing mass flux and increasing outlet quality. In addition, it can be seen from Fig. 8 (top) that the saturation pressure does not affect the heat transfer coefficient significantly. A decrease in heat transfer coefficient with increasing pressure can be seen in the lower panel in Fig. 8. This decrease is attributed to the fact that the subcooling of the fluid increases with increasing

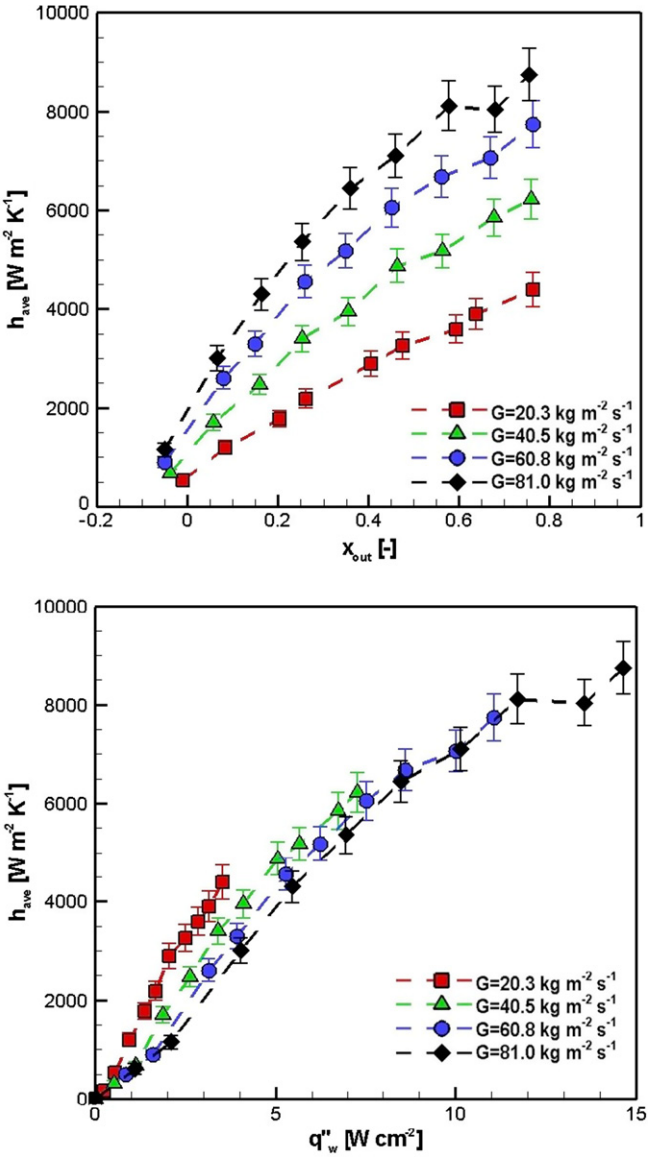

Fig. 7. Heat transfer coefficient in the pre-evaporator at different mass fluxes for a fixed saturation pressure of 550 kPa as a function of outlet vapor quality (top) and heat flux (bottom).

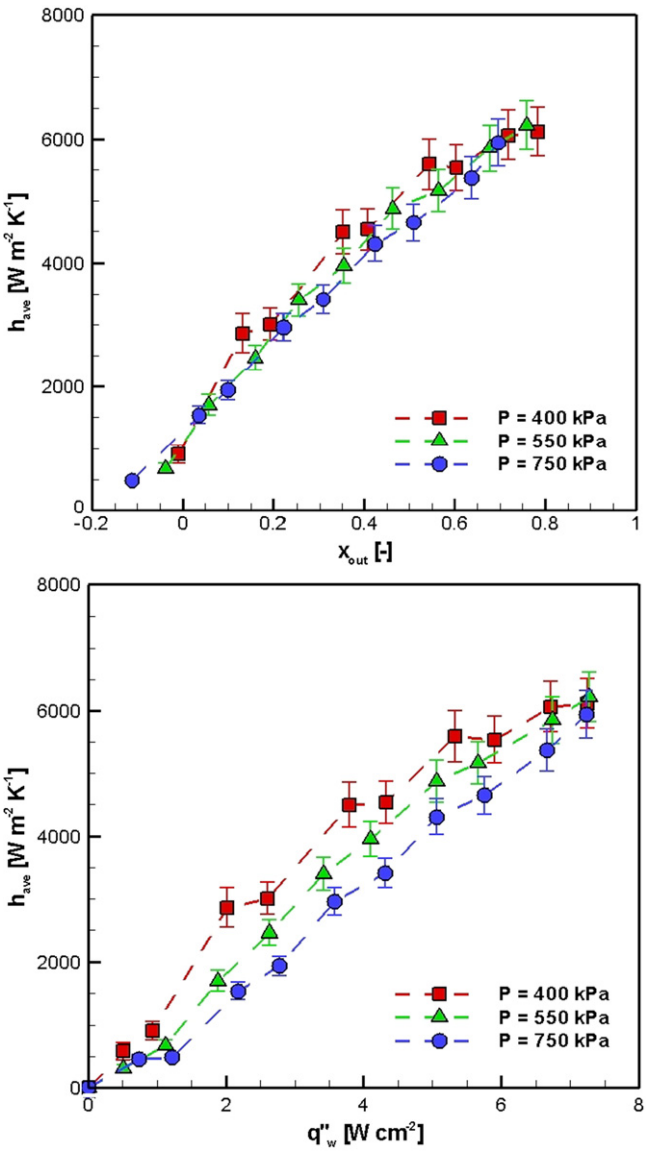

Fig. 8. Heat transfer coefficient in the pre-evaporator at different saturation pressures for a constant refrigerant mass flux of 40.5 kg m^{-2} s^{-1} as a function of outlet vapor quality (top) and heat flux (bottom).

saturation pressures. The constant inlet temperature of 8.3 ± 0.5 °C leads to a larger temperature difference at high saturation temperatures and results in a larger heat transfer coefficient for the lower saturation pressures. When plotting the heat transfer coefficient against outlet quality (Fig. 8 top), this effect is accounted for by the vapor quality calculated from the subcooling. This shows the independence of heat transfer coefficient on saturation pressure and the considerable influence of subcooling on the heat transfer measurements.

Finally, the plot of heat transfer coefficient versus heat flux at constant pressure (Fig. 7 bottom) shows an interesting result. The heat transfer coefficient is seen to decrease marginally with increasing mass flow rate. A closer evaluation shows that the outlet quality at low mass flow rates at any specific heat flux is higher than for high mass flow rates. Higher outlet quality also implies improved heat transfer. Therefore, it may be concluded that the effect of mass flow rate on heat transfer coefficient is smaller than the effect of heat flux.

3.5. Heat transfer coefficients as a function of local quality

As has been noted, the pressure drop over the test section assembly consisting of pre-evaporator, test piece, and post-evaporator was always below 0.3 kPa, due to the low mass flow rates in the experiments. This pressure drop corresponds to a change in saturation temperature of approximately 0.2 °C. Therefore, the saturation temperature of the refrigerant was assumed to be constant over the test piece which is only one-tenth of the length of the test section assembly. The saturation temperature was

calculated using the mean pressure between the inlet and outlet.

Repeatability of the measurements was verified by conducting multiple tests over a period of time; the test section was completely disassembled and then re-assembled each time. Two such sets of results are shown here. In the first set, data points were obtained for vapor qualities of approximately −0.2, 0.0, 0.2, 0.4, 0.6, and 0.8, while in the second, additional data points were obtained at qualities of approximately −0.1, 0.1, 0.3, 0.5, and 0.7. Figs. 9 and 10 show that both sets of results follow the same trend, with the trendline being indistinguishable to within the measurement uncertainty.

Fig. 9 shows the local heat transfer coefficient at a fixed saturation pressure of 550 kPa for four refrigerant mass flow rates as a function of vapor quality. Each point in the figure represents the heat transfer coefficient measured for a vapor quality change of 20% (±1%) across the test piece. For instance, a point shown as being at 30% quality implies the average heat transfer coefficient over the thermodynamic quality range of 20–40%. The differential of 20% in vapor quality across the test piece was chosen as a compromise between measurement uncertainty and resolution. Fig. 10 shows the heat transfer coefficient determined as outlined above but for a constant mass flux of 40.5 kg m^{-2} s^{-1} with respect to the average thermodynamic quality over the test piece. The results are presented for three different pressures of 400, 550, and 750 kPa. All measurement uncertainties calculated by error propagation are within an error band of 13%.

The heat transfer coefficient is seen to increase with increasing mass flux. Increasing mass flux also means increasing heat flux, due to the operating conditions discussed earlier. The heat fluxes at the four mass fluxes of

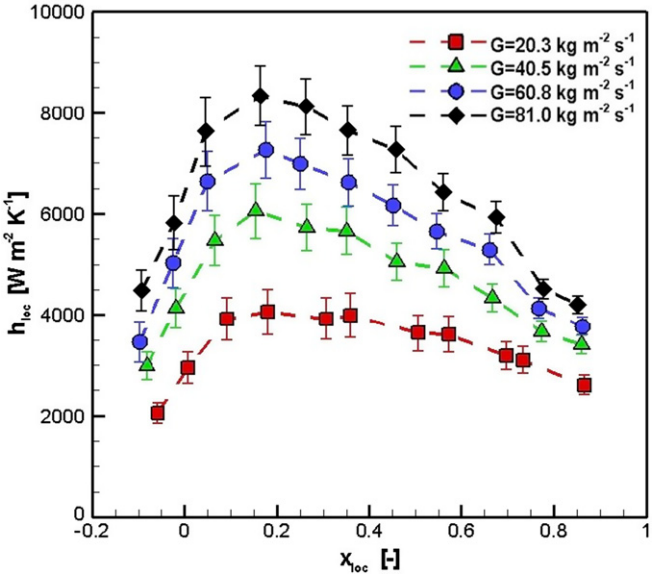

Fig. 9. Heat transfer coefficient (based on wetted heated area) at a fixed saturation pressure of 550 kPa and four different mass fluxes as a function of vapor quality.

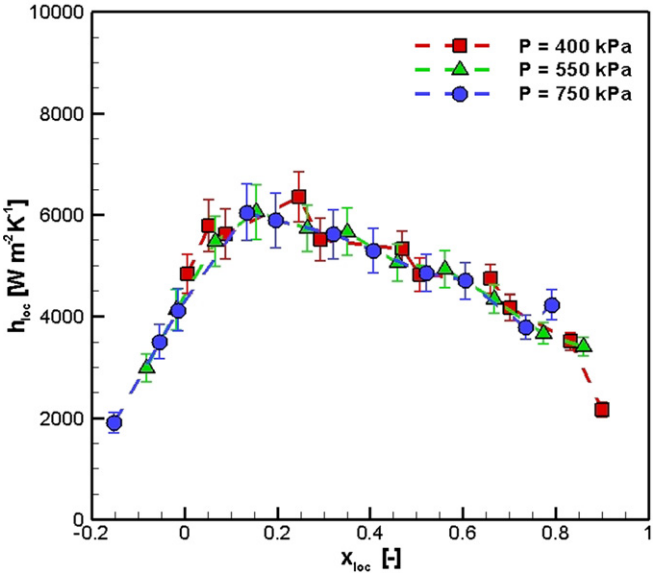

Fig. 10. Heat transfer coefficient (wetted heated area) at a fixed refrigerant mass flux of 40.5 kg m^{-2} s^{-1} and three different saturation pressures as a function of vapor quality.

20.3, 40.5, 60.8, and 81.0 kg m^{-2} s^{-1} are 2.5, 5.0, 7.5, and 10 W cm^{-2}, respectively, with an uncertainty of less than 2.1%. The effect of saturation pressure on the heat transfer coefficient is negligible within the range of operating conditions considered, since the results cannot be distinguished within the measurement uncertainty. As expected, there is a strong increase in the heat transfer coefficient at low vapor qualities. The maximum heat transfer coefficient occurs at a vapor quality of 20%. As vapor quality increases, the heat transfer coefficient decreases. This is consistent with the results reported in [27,17]. While the general trend of variation in the heat transfer coefficient with vapor quality was expected, the peak in heat transfer coefficient occurs at lower vapor qualities in the microchannels considered here compared to results for larger-diameter tubing in Wojtan et al. [28]. The difference in heat transfer behavior between parallel microchannels and conventional-sized channels seems to be influenced by confinement of the bubbles in the microchannels, as well as differences in flow patterns and flow instabilities especially in multiple parallel channels. Visual observation revealed that for most of the measurements presented in this work of heat transfer versus vapor quality, the flow regimes could best be described as slug or intermittent flow. Only at very high vapor qualities ($x > 0.7$) was annular flow observed.

4. Conclusions

A carefully designed experimental test setup has been constructed to measure the local flow boiling heat transfer coefficient of refrigerant HFC-134a in a copper microchannel cold plate evaporator. The microchannel evaporator consists of 17 parallel channels each with a hydraulic diam-

eter of 1.089 mm and an aspect ratio of 2.5. Excellent energy balance was achieved with the instrumentation deployed; the measured single-phase heat transfer coefficients also agreed with predictions from correlations in the literature to within the measurement uncertainty. The experiments were also shown to be repeatable. The maximum measurement uncertainty in the heat transfer coefficient was found to be less than 13%.

During the experiments, the mass flux was varied from 20.3 to 81.0 $kg\,m^{-2}\,s^{-1}$ corresponding to flow rates of 0.5–2 $g\,s^{-1}$ at pressures of 400–750 kPa. Qualities at the inlet to the test piece were varied from subcooled liquid to 80% vapor quality. The heat transfer coefficient varied significantly with refrigerant quality and showed a peak at a vapor quality of 0.2 in all the experiments. The heat transfer coefficient first rises steeply as vapor quality increases from a subcooled value, and again drops sharply with further increases in vapor quality. The influence of saturation pressure on the heat transfer coefficient is almost negligible for the range of values investigated. The heat transfer coefficient increases strongly with increasing mass flow rate and the corresponding increase in heat flux. These results are in contrast to those obtained for larger channels in the literature. The strong dependence of the heat transfer coefficient on heat flux is consistent with other reports for microchannels.

Acknowledgements

The authors acknowledge the financial support from members of the Cooling Technologies Research Center (www.ecn.purdue.edu/CTRC), a National Science Foundation Industry/University Cooperative Research Center at Purdue University.

References

[1] S.V. Garimella, C.B. Sobhan, Transport in microchannels – a critical review, Ann. Rev. Heat Transfer 13 (2003) 1–50.
[2] J.R. Thome, Boiling in microchannels: a review of experiment and theory, Int. J. Heat Fluid Flow 25 (2004) 128–139.
[3] S.V. Garimella, V. Singhal, D. Liu, On-chip thermal management with microchannel heat sinks and integrated micropumps, Proc. IEEE 94 (2006) 1534–1548.
[4] A. Bar-Cohen, E. Rahim, Modeling and prediction of two-phase refrigerant flow regimes and heat transfer characteristics in microgap channels, in: Proceedings of the 5th International Conference on Nanochannels, Microchannels, and Minichannels ICNMM2007, 2007.
[5] G. Hetsroni, D. Klein, A. Mosyak, Z. Segal, E. Pogrebnyak, Convective boiling in parallel microchannels, Microscale Thermophys. Eng. 8 (2004) 403–421.
[6] D. Liu, P. Lee, S.V. Garimella, Prediction of the onset of nucleate boiling in microchannel flow, Int. J. Heat Mass Transfer 48 (2005) 4149–5134.
[7] W. Qu, I. Mudawar, Transport phenomena in two-phase microchannel heat sinks, J. Electron. Pack. 126 (2004) 213–224.
[8] P.S. Lee, S.V. Garimella, Saturated flow boiling heat transfer and pressure drop in silicon microchannel arrays, Int. J. Heat Mass Transfer, Available online 28 June 2007.
[9] M.E. Steinke, S.G. Kandlikar, An experimental investigation of flow boiling characteristics of water in parallel microchannels, Trans. ASME 126 (2004) 518–526.
[10] K.H. Chang, C. Pan, Two-phase flow instability for boiling in a microchannel heat sink, Int. J. Heat Mass Transfer 50 (11–12) (2007) 2078–2088.
[11] H.Y. Wu, P. Cheng, Visualization and measurements of periodic boiling in silicon microchannels, Int. J. Heat Mass Transfer 14 (2003) 2603–2614.
[12] S. Trutassanawin, E.A. Groll, S.V. Garimella, L. Cremaschi, Experimental investigation of a miniature-scale refrigeration system for electronics cooling, IEEE Trans. Compon. Pack. Technol. 29 (2006) 678–687.
[13] R. Mongia, K. Masahiro, E. DiStefano, Small scale refrigeration system for electronics cooling within a notebook computer, in: Proceedings of the ITHERM'06, 2006.
[14] P.E. Phelan, J. Swanson, F. Chiriac, V. Chiriac, Designing a mesoscale vapor compression refrigerator for cooling high-power microelectronics, in: Proceedings of the ITHERM'04, 2004.
[15] G.M. Lazarek, S.H. Black, Evaporative heat transfer, pressure drop and critical heat flux in a small vertical tube with R-113, Int. J. Heat Mass Transfer 25 (7) (1982) 945–960.
[16] T.N. Tran, M.W. Wambsganss, D.M. France, Small circular and rectangular channel boiling with two refrigerants, Int. J. Multiphase Flow 22 (1996) 485–498.
[17] Y. Yan, T. Lin, Evaporation heat transfer and pressure drop of refrigerant R-134a in a small pipe, Int. J. Heat Mass Transfer 41 (1998) 4183–4194.
[18] S. Lin, P.A. Kew, K. Cornwell, Two-phase heat transfer to a refrigerant in a 1 mm diameter tube, Int. J. Refrig. 24 (2001) 51–56.
[19] H.J. Lee, S.Y. Lee, Heat transfer correlation for boiling flows in small rectangular horizontal channels with low aspect ratios, Int. J. Multiphase Flow 27 (2001) 2043–2062.
[20] S. Saitoh, H. Daiguji, E. Hihara, Effect of tube diameter on boiling heat transfer of R-134a in horizontal small-diameter tubes, Int. J. Heat Mass Transfer 48 (2005) 4473–4984.
[21] M.E. Steinke, S.G. Kandlikar, Flow boiling and pressure drop in parallel flow microchannels, in: Proceedings of the First International Conference on Microchannels and Minichannels, 2003.
[22] J.R. Taylor, An Introduction to Error Analysis, second ed., University Science Books, 1997.
[23] S.E. Churchill, A comprehensive correlating equation for laminar, assisting, forced and free convection, Am. Inst. Chem. Eng. AIChE J. 23 (1) (1977) 10–16.
[24] E.N. Sieder, G.E. Tate, Heat transfer and pressure drop of liquids in tubes, Indust. Eng. Chem. 28 (1936) 1429–1435.
[25] D. Liu, S.V. Garimella, Flow boiling heat transfer in microchannels, ASME J. Heat Transfer 129 (10) (2007) 1321–1332.
[26] L. Tadrist, Review on two-phase flow instabilities in narrow spaces, Int. J. Heat Fluid Flow 28 (2007) 54–62.
[27] V. Dupont, J.R. Thome, A.M. Jacobi, Heat transfer model for evaporation in microchannels: Part II. Comparison with the database, Int. J. Heat Mass Transfer 47 (14–16) (2004) 3387–3401.
[28] L. Wojtan, T. Ursenbacher, J.R. Thome, Investigation of flow boiling in horizontal tubes: Part II. Development of a new heat transfer model for stratified-wavy, dryout and mist flow regimes, Int. J. Heat Mass Transfer 48 (14) (2005) 2970–2985.
[29] D.B. Tuckerman, R.F.W. Pease, High-performance heat sinking for VLSI, IEEE Electr. Dev. Lett. EDL-2 (5) (1981) 126–129.
[30] M. Molki, P. Mahendra, V. Vengala, Visualization and modeling of flow boiling of R-134a in minichannels with transverse ribs, Heat Transfer Eng. 25 (2004) 94–103.
[31] J. Lee, I. Mudawar, Two phase flow in high-heat flux micro-channel heat sink for refrigeration cooling applications: Part I – pressure drop characteristics, Int. J. Heat Mass Transfer 48 (2005) 928–940.
[32] J. Lee, I. Mudawar, Two phase flow in high-heat flux micro-channel heat sink for refrigeration cooling applications: Part II – heat transfer characteristics, Int. J. Heat Mass Transfer 48 (2005) 941–955.

[33] P. Lee, S.V. Garimella, D. Liu, Investigation of heat transfer in rectangular microchannels, Int. J. Heat Mass Transfer 48 (2005) 1688–1704.
[34] Y.M. Lie, T.F. Lin, Saturated flow boiling heat transfer and associated bubble characteristics of R-134a in a narrow annular duct, Int. J. Heat Mass Transfer 48 (2005) 5602–5615.
[35] T. Chen, S.V. Garimella, Measurements and high-speed visualization of flow boiling of a dielectric fluid in a silicon microchannel heat sink, Int. J. Multiphase Flow 32 (2006) 957–971.
[36] Y.M. Lie, T.F. Lin, Subcooled flow boiling heat transfer and associated bubble characteristics of R-134a in a narrow annular duct, Int. J. Heat Mass Transfer 49 (2006) 2077–2089.
[37] T. Yen, M. Shoji, F. Takemura, Y. Suzuki, N. Kasagi, Visualization of convective boiling heat transfer in single microchannels with different shaped cross-sections, Int. J. Heat Mass Transfer 49 (2006) 3884–3894.
[38] R. Yun, J.H. Heo, Y. Kim, Evaporative heat transfer and pressure drop of R410A in microchannels, Int. J. Refrig. 29 (2006) 92–100.
[39] B. Schneider, A. Kosar, Y. Peles, Hydrodynamic cavitation and boiling in refrigerant (R-123) flow inside microchannels, Int. J. Heat Mass Transfer 50 (2007) 2838–2854.